Rock Mech Rock Eng
DOI 10.1007/s00603-011-0206-x

ORIGINAL PAPER

An Experimental Study of the Fracture Coalescence Behaviour of Brittle Sandstone Specimens Containing Three Fissures

S. Q. Yang · D. S. Yang · H. W. Jing · Y. H. Li · S. Y. Wang

Received: 26 April 2011 / Accepted: 18 November 2011

Abstract To analyse the fracture coalescence behaviour of rock, rectangular prismatic sandstone specimens (80 × 160 × 30 mm in size) containing three fissures were tested under uniaxial compression. The strength and deformation behaviours of the specimens are first analysed by investigating the effects of the ligament angle β_2 on the peak strength, peak strain and crack initiation stress of the specimens. To confirm the sequence of crack coalescence, a photographic monitoring technique is used throughout the entire period of deformation. Based on the results, the relationship between the real-time crack coalescence process and the axial stress–strain curve of brittle sandstone specimens is also developed, and this relationship can be used to evaluate the macroscopic deformation characteristics of pre-cracked rock. The equivalent strain evolution fields of the specimen, with $\alpha = \beta_1 = 45°$ and $\beta_2 = 90°$, are obtained using the digital image correlation technique and show good agreement with the experimental results of pre-cracked brittle sandstone. These experimental results are expected to improve the understanding of fracture mechanisms and be used in rock engineering with intermittent structures, such as deep underground excavated tunnels.

Keywords Brittle sandstone · Three fissures · Deformation · Crack coalescence · Photographic monitoring

1 Introduction

Rock is a complicated geological medium that usually contains flaws such as joints, fissures, faults and weak surfaces. Under an applied load, new cracks are readily initiated at the tips of nearby pre-existing flaws, and these new cracks propagate along the direction of axial stress in the rock (Li et al. 2005; Wong and Einstein 2009a, b; Park and Bobet 2009; Yang and Jing 2011), resulting in an unstable failure due to crack coalescence. With the increase of engineering scales, rock masses transform from an intact state to a heavily fractured rock mass (Fig. 1) (Hoek 1998). As a result, the mechanical behaviour of intact rock can rarely be used to characterise the strength and deformation characteristics of fractured rock masses. Therefore, experimental and numerical investigations are conducted for fractured rock containing flaws in order to determine the stability and safety of rock masses in applications such as deep underground engineering and rock engineering for nuclear waste disposition (Hoek 1998; Prudencio and Van Sint Jan 2007; Lee and Jeon 2011).

For rock-like material, pre-existing fissures can be easily fabricated by inserting mica, paper or thin steel discs to simulate open or closed fissures. Wong et al. (2001) conducted uniaxial compression tests for rock-like materials containing three closed flaws to investigate the crack coalescence and peak strength behaviours of fractured rock.

S. Q. Yang (✉) · H. W. Jing · Y. H. Li
State Key Laboratory for Geomechanics and Deep Underground Engineering, School of Mechanics and Civil Engineering, China University of Mining and Technology, Xuzhou 221008, People's Republic of China
e-mail: yangsqi@hotmail.com

D. S. Yang
Laboratoire de Mécanique des Solides, Ecole Polytechnique de Paris, Palaiseau cedex 91128, France

S. Y. Wang
Center for Geotechnical and Materials Modelling, The University of Newcastle, University Drive, Callaghan, NSW 2238, Australia

Published online: 20 December 2011

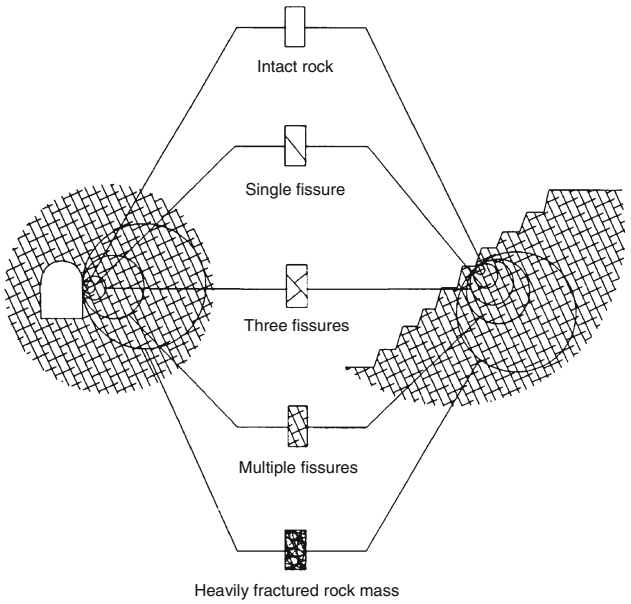

Fig. 1 Idealised diagram showing the transition from an intact state to a heavily fractured rock mass, with increasing specimen scale (Hoek 1998)

Their results show that the mechanisms of crack coalescence depend on the flaw arrangement and the frictional coefficient on the flaw surface. To enable a comparison with experimental results, Tang et al. (2001) used uniaxial compression to investigate the failure mechanism and crack coalescence modes, based on the RFPA^{2D} code, of a rock-like material containing three flaws. Their numerical results agree with most of the phenomena observed in actual experiments, such as the initiation and growth of wing and secondary cracks, crack coalescence and macro-failure of the specimen. However, despite similar flaw geometries and loading conditions, the crack coalescence behaviours of rock-like materials and natural rock are different because of the complexity of natural rock material (Wong and Einstein 2009a, b). Wong and Einstein (2009a, b) summarised the effects of the flaw angle, ligament angle and length on the cracking processes and coalescence patterns of Carrara marble specimens with dimensions of 76 × 152 × 32 mm and containing two open fissures, and used a high-speed camera to observe the specimens at a macroscopic scale. Feng et al. (2009) experimentally investigated the mechanism of multi-crack interaction in limestone specimens containing three fissures of different arrangements, using coupled uniaxial compressive stress and chemical solutions with different ionic concentrations and pH values. The limestone specimens were small, with dimensions of 15 × 30 × 3 mm. The acoustic emission (AE) technique has been widely applied in many past studies to investigate the damage and fracture behaviour of internal brittle rock material, but the AE technique was less often used to explore the crack coalescence of brittle rock containing pre-existing fissures under uniaxial compression (Chang and Lee 2004; Debecker and Vervoort 2009; Tham et al. 2005). Yang and Jing (2011) conducted uniaxial compression experiments with brittle sandstone specimens of dimensions 60 × 120 × 30 mm and containing a single fissure to investigate the influences of fissure length and angle on the strength and deformation failure behaviour of specimens by using photographic monitoring and AE techniques.

However, the relationship between the real-time crack coalescence process using photographic monitoring and the axial stress–strain curve of rock material has, so far, not been investigated for brittle sandstone specimens containing three pre-existing fissures. Therefore, in this research, to better understand the strength failure and crack coalescence phenomena in fractured rock, a rock mechanics servo-controlled testing system was used to conduct uniaxial compression tests with brittle sandstone specimens containing three fissures. Moreover, a photographic monitoring technique was used to obtain the relationship between the real-time crack coalescence process and the axial stress–strain behaviour for brittle sandstone containing three fissures. The emphasis of this research was to investigate the effects of the ligament angle on the strength and deformation failure behaviours of a brittle sandstone material containing three fissures and to analyse the real-time crack coalescence process in a sandstone material under uniaxial compression, using a photographic monitoring technique.

2 Specimen Preparation and Testing Procedure

2.1 Sandstone Material and Sample Preparation

Sandstone specimens from Linyi City, Shandong province, China, were used in the experiments. The mineral components of the sandstone material were feldspar, quartz and detritus (Fig. 2). The sandstone, a fine-grained heterogeneous material, had crystalline and blocky features, and an average unit weight of about 2,650 kg/m^3.

Rectangular prismatic specimens of sandstone, with dimensions of 80 × 160 × 30 mm, were prepared. All specimens had a height-to-width ratio of 2.0 to ensure a uniform stress state within the central part of the specimens. The geometry of the specimens containing three fissures is described in Fig. 3. The term “fissure” is used to describe an artificially created flaw; however, the term “crack” is adopted to describe a new fracture that forms during loading. The geometry of the three fissures is defined by six geometrical parameters: fissure length $2a$, ligament length $2b_1$ between fissures ① and ②, ligament length $2b_2$ between fissures ① and ③, fissure angle α (the angle of the fissure to

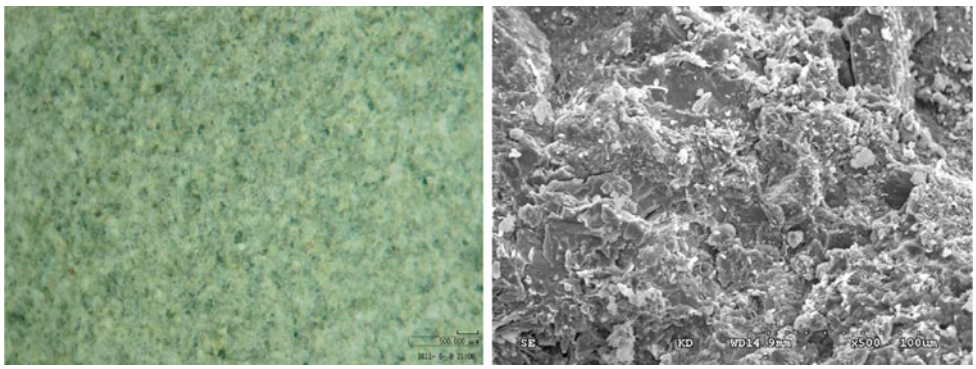

Fig. 2 Microscopic features of the sandstone material used in this study

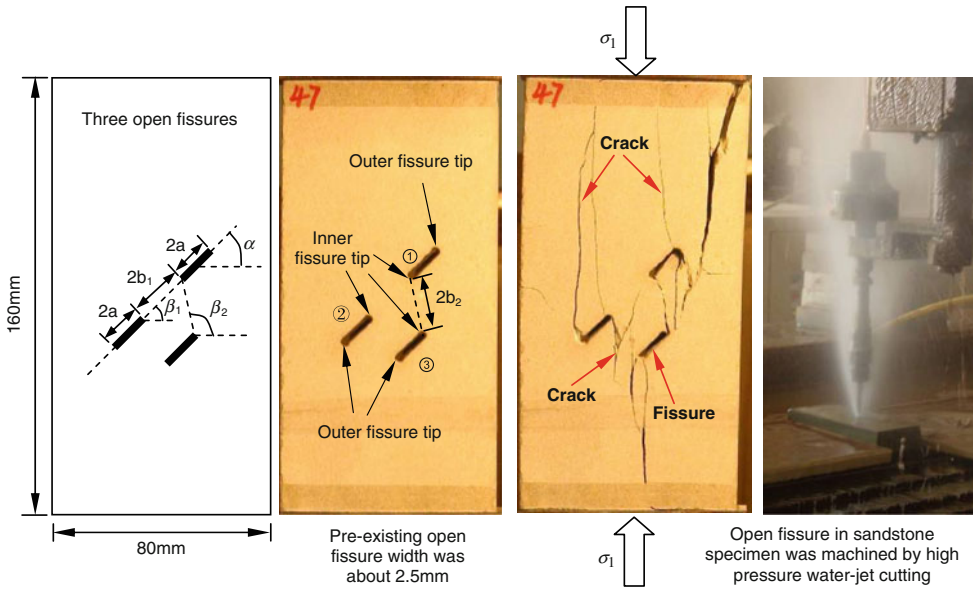

Fig. 3 Geometry of the three fissures in the sandstone specimens. α is the fissure angle, β_1 is the ligament angle between fissures ① and ②, β_2 is the ligament angle between fissures ① and ③, $2a$ is the fissure length, $2b_1$ is the ligament length between fissures ① and ②, and $2b_2$ is the ligament length between fissures ① and ③. In this research, three open fissures were machined in sandstone specimens by high-pressure water jet cutting

the horizontal direction), ligament angle β_1 between fissures ① and ②, and ligament angle β_2 between fissures ① and ③, as shown in Fig. 3. Fissure ① and ② are coplanar, and fissures ①, ② and ③ are parallel, as shown in Fig. 3.

A high-pressure water jet cutting machine (Yang and Jing 2011) was used to cut three fissures in intact specimens. The machined open fissure widths are approximately 2.5 mm. To investigate the effects of the geometry of three pre-existing fissures on the fracture coalescence behaviour of sandstone under uniaxial compression, different fissure geometries are designed by varying β_2 while holding the other five parameters as constant values ($2a = 15$ mm, $2b_1 = 2b_2 = 20$ mm and $\alpha = \beta_1 = 45°$). A detailed description of the sandstone specimens containing three fissures is listed in Table 1.

2.2 Testing Procedure

Uniaxial compression tests for intact and flawed sandstone specimens containing three fissures were conducted using a rock mechanics servo-controlled testing system. The axial stress was imposed on the surface of the rock specimen until failure. All tests were conducted under displacement-controlled conditions with a strain rate of 8.125×10^{-6}/s. During the uniaxial compression experiment, the loads and deformations of the specimens were recorded simultaneously. Moreover, two rigid steel blocks, with dimensions $33 \times 83 \times 15$ mm, were placed between the loading frame and the rock specimen. Two anti-friction gaskets were placed between the two rigid steel blocks and the end faces of the rock specimens to reduce the end-friction effects for specimens with a height-to-width ratio of approximately 2.0.

3 Analysis of Experimental Results

3.1 Axial Stress–Strain Curve of Intact Specimens

Figure 4 presents the axial stress–strain curve of intact sandstone specimens under uniaxial compression. The corresponding cracking process is also captured by photographic monitoring, as shown in Fig. 5. The letters in

Table 1 Sandstone specimens containing three fissures under uniaxial compression

Specimen	W (mm)	H (mm)	T (mm)	α (°)	β_1 (°)	β_2 (°)	$2a$ (mm)	$2b_1$ (mm)	$2b_2$ (mm)	Note
B0r#	80.8	158.9	31.4	N/A	N/A	N/A	N/A	N/A	N/A	Intact specimen
B45#	80.6	159.5	29.8	45	45	75	15	20	20	Flawed specimen containing three open fissures
B46#	81.0	160.0	31.2	45	45	90	15	20	20	
B47#	80.5	159.1	29.8	45	45	105	15	20	20	
B48#	80.1	159.2	29.8	45	45	120	15	20	20	
B56#	80.9	156.5	31.2	45	45	120	15	20	20	

W width, H height, T thickness

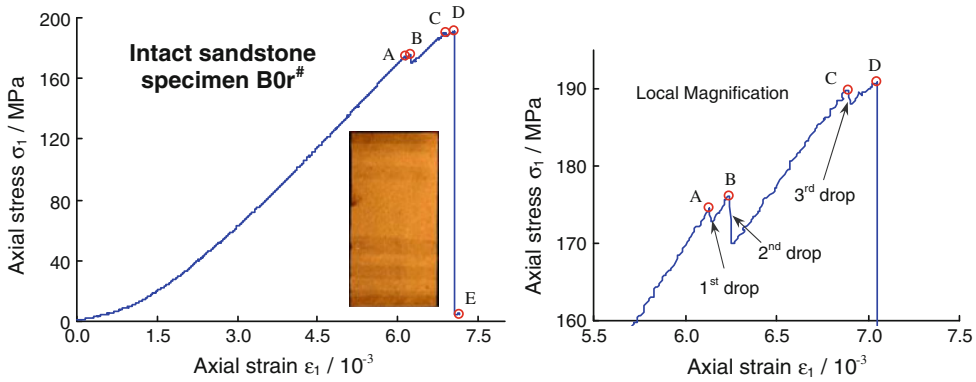

Fig. 4 Axial stress–strain curve of an intact sandstone specimen under uniaxial compression

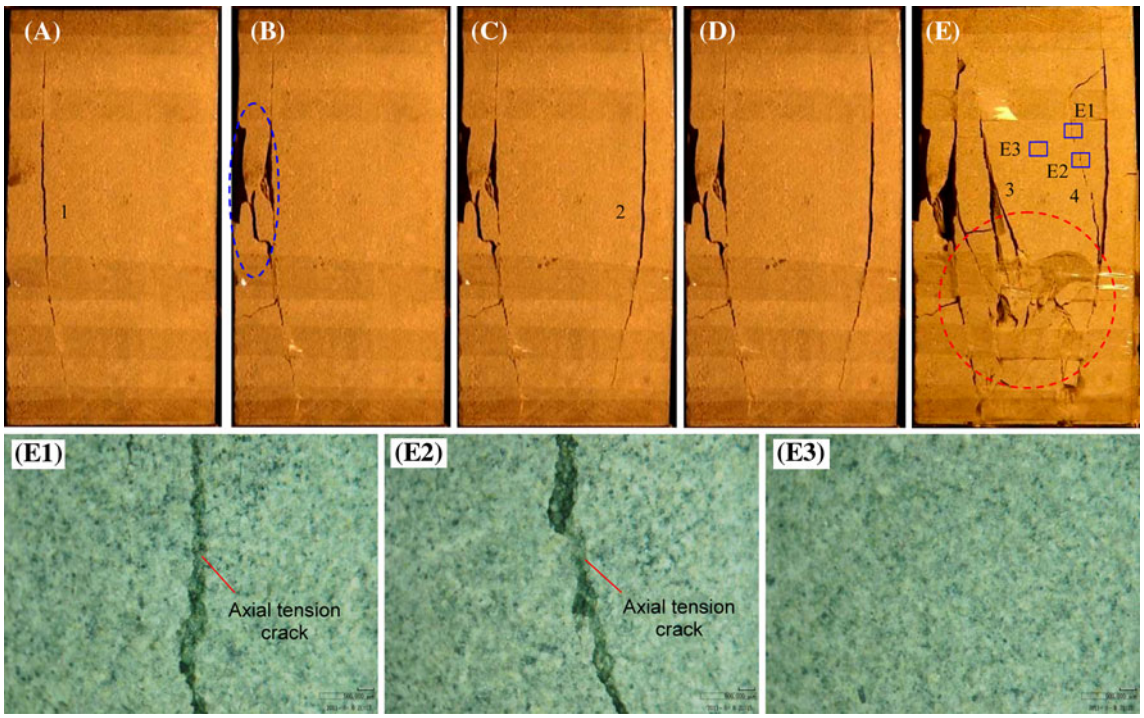

Fig. 5 Crack coalescence process of an intact sandstone specimen under uniaxial compression

Fig. 4 correspond to those shown in Fig. 5. Table 2 lists the peak strength σ_c and the peak axial strain ε_{1c} for intact specimens under uniaxial compression.

In accordance with Figs. 4 and 5, crack coalescence in the intact specimen can not be observed by unaided eyes before point A ($\sigma_1 = 174.46$ MPa $= 91.4\%\sigma_c$). However,

Table 2 Mechanical parameters of intact and flawed sandstone specimens containing three fissures under uniaxial compression

Specimen	α (°)	β_1 (°)	β_2 (°)	$2a$ (mm)	$2b_1$ (mm)	$2b_2$ (mm)	ε_{1c} ($\times 10^{-3}$)	σ_c (MPa)	D_a
B0r#	Intact sandstone specimen						7.051	190.8	0.000
B45#	45	45	75	15	20	20	4.568	87.17	0.543
B46#	45	45	90	15	20	20	4.464	73.87	0.613
B47#	45	45	105	15	20	20	3.387	79.71	0.582
B48#	45	45	120	15	20	20	4.254	101.86	0.466
B56#	45	45	120	15	20	20	4.100	101.36	0.469

when the axial stress is loaded to point A, the first crack (vertical splitting tensile failure) rapidly propagates along the direction of axial loading, which causes the axial stress to drop to 172.8 MPa in an approximately constant axial strain. After the first stress drop and with the increasing deformation, the axial stress is loaded to point B ($\sigma_1 = 176.06$ MPa $= 92.3\%\sigma_c$); some surface failures and short cracks occur near crack 1, as shown in the elliptical region of Fig. 5b. At this moment, the second stress drop occurs, falling from 176.06 to 170 MPa in an approximately constant axial strain. Afterwards, the axial supporting capacity slowly increases with the increasing deformation because the specimen still had a good supporting structure. When the specimen reaches an axial stress of approximately 189.8 MPa (point C, $99.5\%\sigma_c$), crack 2 (vertical splitting tensile failure) forms quickly along the direction of axial stress, which leads to the third stress drop, from 189.8 to 188.1 MPa, as shown in Fig. 4. Continuously increasing the axial displacement causes the specimen to quickly reach point D ($\sigma_1 = 190.8$ MPa $= 100\%\sigma_c$). During this process, the axial stress–strain curve departs notably towards the strain axis because of obvious damage of the supporting structure, but no new cracks are observed. However, after the peak stress, the specimen undergoes brittle failure, and the axial stress drops abruptly to 4.4 MPa in additional cracks (e.g. cracks 3–4), as shown in Fig. 5e. During the ultimate drop, a large failure sound can be heard.

In accordance with the above description, the axial stress–strain behaviour of rock materials is an external response and has a notable relation with the real-time crack coalescence process. However, for some hard and brittle rocks, the real-time crack coalescence process, similar to that shown in Fig. 5, is usually difficult to capture because of the abrupt brittle failure of rock specimens.

3.2 Axial Stress–Strain Curve of Flawed Specimens Containing Three Fissures ($\alpha = \beta_1 = 45°$)

Figure 6 shows the complete axial stress–strain curves for sandstone specimens containing three fissures ($\alpha = \beta_1 = 45°$) under uniaxial compression. These curves are different from those of intact specimens, as shown in Fig. 4. Compared with intact specimens, more stress drops are observed in the axial stress–strain curves as a result of the coalescence of new cracks in flawed specimens with the increasing deformation. The relationship between the real-time crack coalescence process and the axial stress–strain curve of brittle sandstone specimens containing three fissures will be depicted in the fourth section of this article. Here, only the axial stress–strain curve behaviour of flawed specimens containing three fissures is discussed.

Figure 7 shows the effect of heterogeneity on the axial stress–strain curves of sandstone specimens containing three fissures ($\alpha = \beta_1 = 45°$, $\beta_2 = 120°$) under uniaxial compression. From Fig. 7, it can be seen that, for flawed specimens containing three fissures with the same geometry, the axial stress–strain curves exhibit a very good consistency. The peak strengths of the two specimens B48# and B56# are 101.86 and 101.36 MPa, respectively, while the corresponding peak axial strains of the same two specimens are 4.254 and 4.100×10^{-3}, respectively. Based on the above analysis, we can see that the heterogeneity has nearly no effect on the axial stress–strain curves of flawed specimens containing three fissures with the same geometry. Therefore, in this research, the experimental results in Fig. 6 can be used to discuss the effects of the ligament angle β_2 on the strength and deformation parameters of the specimen.

To show clearly the effect of the ligament angle β_2 on the axial stress–strain curves of the specimen, four axial stress–strain curves (Fig. 6) were plotted together in Fig. 8. The corresponding peak strength and peak axial strain of the specimens are also listed in Table 2.

From Table 2, the peak strength and peak axial strain of flawed specimens are lower than those of the intact specimen, and the extent of this reduction is significantly related to the ligament angle β_2. Figure 9 shows the influence of β_2 on the peak strength and peak strain of the specimens. Note that, in Fig. 9, only the mechanical parameter of specimen B48#, as shown in Fig. 7, is used.

To indicate the reduction extent of the peak strength of flawed specimens containing three fissures in relation to intact specimens, the reduction factor was defined as follows:

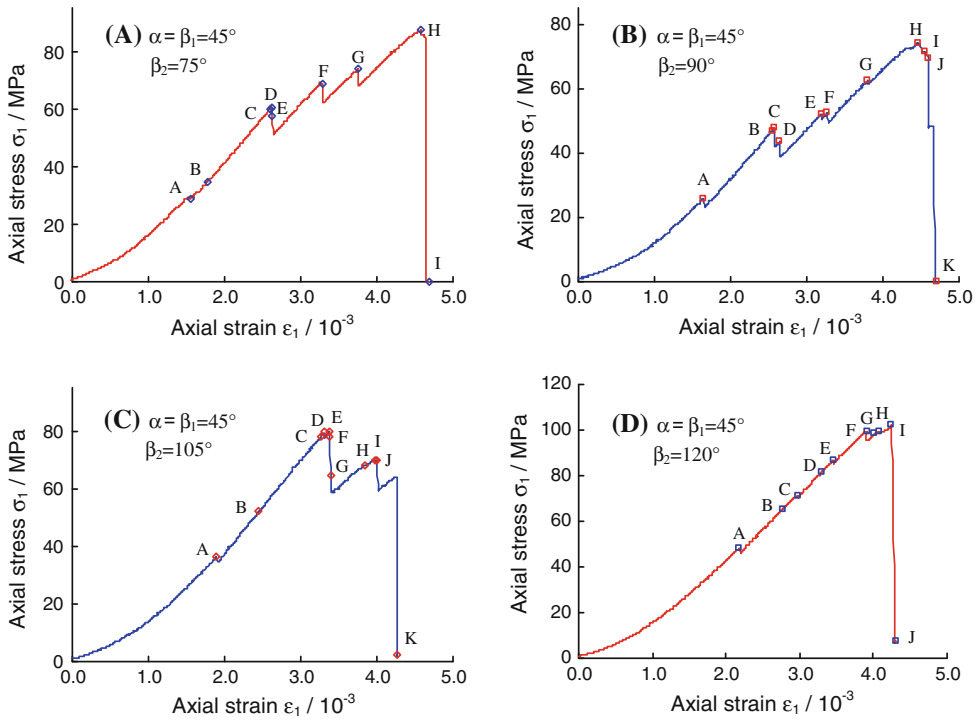

Fig. 6 Complete axial stress–strain curves of sandstone specimens containing three fissures ($\alpha = \beta_1 = 45°$) under uniaxial compression

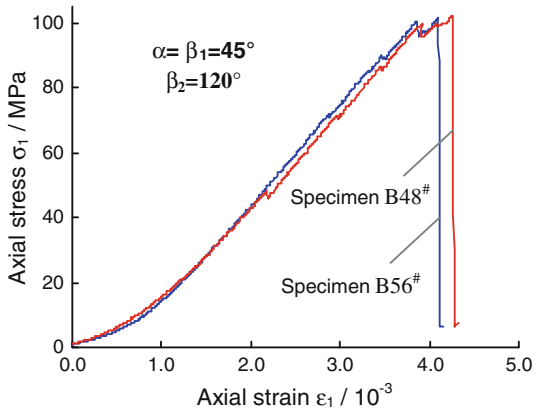

Fig. 7 Effect of heterogeneity on the axial stress–strain curves of sandstone specimens containing three fissures under uniaxial compression

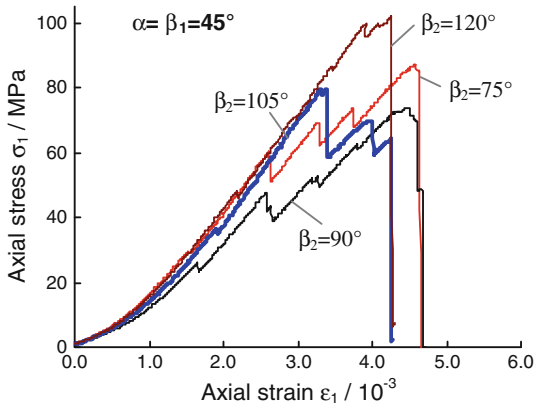

Fig. 8 Effect of the ligament angle β_2 on the axial stress–strain curves of sandstone specimens containing three fissures under uniaxial compression

$$D_{at} = \frac{\sigma_{cm} - \sigma_{cn}}{\sigma_{cm}} \quad (1)$$

where σ_{cm} is the peak strength of an intact specimen, equal to 190.8 MPa in the present study, and σ_{cn} is the peak strength of a flawed specimen containing three fissures. In accordance with Eq. 1, the calculated D_{at} values of flawed specimens containing three fissures are also listed in Table 2.

As indicated in Table 2, the D_{at} value of the specimen with three fissures of $\beta_2 = 90°$ is the highest of the four specimens containing three fissures (with $\alpha = \beta_1 = 45°$), indicating that the peak strength of the specimen with three

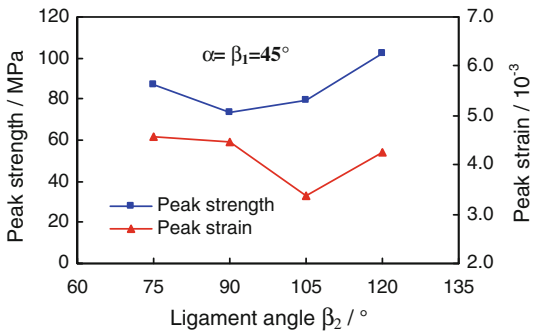

Fig. 9 Influence of the ligament angle β_2 on the peak strength and peak strain of sandstone specimens containing three fissures under uniaxial compression

fissures of $\beta_2 = 90°$ is the lowest ($\sim$73.87 MPa) under uniaxial compression. As β_2 decreases from 90° to 75°, the D_{at} value of the flawed specimens decreases from 0.613 to 0.543. However, the D_{at} value of the flawed specimens also decreases from 0.613 to 0.466 as β_2 increases from 90° to 120°. The above analysis reveals that the uniaxial compressive strength first decreases and then increases as the ligament angle β_2 is increased in the range from 75° to 120°, as shown in Fig. 9.

The intact sandstone specimen fails at a strain of 0.705% under uniaxial compression, while the sandstone specimens containing three fissures fail at a strain of approximately 0.34–0.46%, which is less than that of the intact specimen. Moreover, the peak axial strain ε_{1c} of the sandstone specimens depends on the ligament angle β_2. As shown in Fig. 9, ε_{1c} is non-linearly related to β_2. As β_2 increases from 75° to 90°, ε_{1c} decreases slightly from 4.568 to 4.464×10^{-3}, whereas it decreases substantially from 4.464 to 3.387×10^{-3} as β_2 increases from 90° to 105°. However, ε_{1c} increases from 3.387 to 4.254×10^{-3} as β_2 increases from 105° to 120°. But the effect of β_2 on the peak strain is not synchronous to the effect on the peak strength, as shown in Fig. 9.

4 Crack Initiation Mode and Analysis of the Coalescence Process

4.1 Crack Initiation Mode and Stress Analysis

During deformation, the crack initiation mode and coalescence process of brittle sandstone specimens containing three fissures ($\alpha = \beta_1 = 45°$) are observed using a photographic monitoring technique.

Figure 10 shows the crack initiation mode of the sandstone specimens containing three fissures ($\alpha = \beta_1 = 45°$) under uniaxial compression. From this figure, the effect of the ligament angle β_2 on the crack initiation mode can be analysed. Here, the mode which initiated the first crack (crack 1) is defined as the crack initiation mode. The corresponding axial stress (i.e. the crack initiation stress) is also given in Fig. 10. The axial stress shown in Fig. 10 corresponds to point A in Fig. 6.

As shown in Fig. 10, the crack initiation mode of sandstone specimens containing three fissures ($\alpha = \beta_1 = 45°$) depends on the ligament angle β_2. For $\beta_2 = 75°$, crack 1 is initiated from the inner and outer tips of fissures ② and ③, while no crack is initiated from the inner and outer tips of fissure ①. Notably, crack 1^a is initiated at the inner tip of fissure ②, and crack 1^b is initiated at the outer tip of fissure ③ and propagates along the direction of the major principal stress. However, crack 1^c is initiated from the inner tip of fissure ③ and evolves towards the inner tip of fissure ②. Crack 1^d is initiated from the outer tip of fissure ② and evolves towards the outer tip of fissure ③ along the vertical direction of the pre-existing fissure. Moreover, the coalescence speeds of cracks 1^c and 1^d are lower than those of cracks 1^a and 1^b. This result is likely due to stress field interactions between fissures ② and ③, and it limits the propagation of cracks 1^c and 1^d.

For $\beta_2 = 90°$ and $\beta_2 = 105°$, the crack initiation modes are approximately similar. In these two specimens, the crack initiation mode is different from that of the other two specimens. Crack 1 is initiated from the inner and outer tips of fissures ① and ③, while no crack is initiated from the inner and outer tips of fissure ②. Cracks 1^a and 1^b are initiated from the outer and inner tips of fissure ①, respectively, while cracks 1^c and 1^d are initiated from the inner and outer tips of fissure ③, respectively. The four cracks 1^a–1^d are initiated in the direction vertical to pre-existing fissures ① or ③, and then evolve along the direction of axial stress.

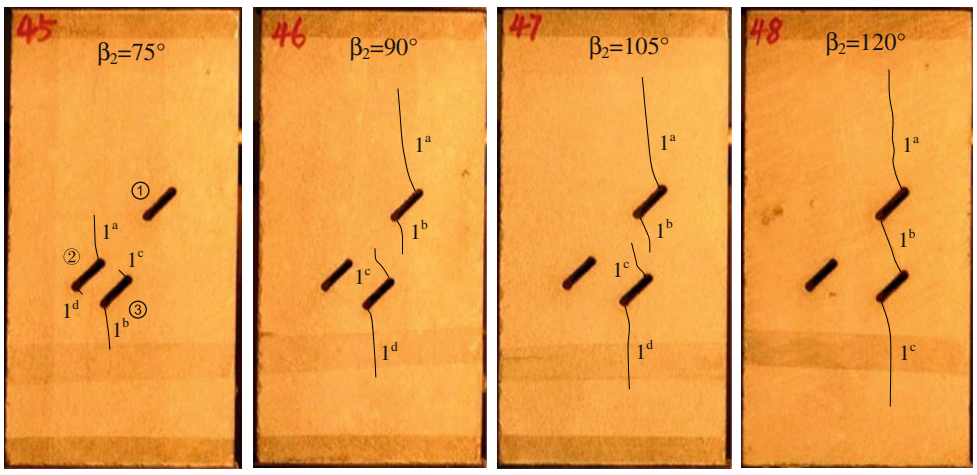

Fig. 10 Crack initiation mode of sandstone specimens containing three fissures ($\alpha = \beta_1 = 45°$) under uniaxial compression

For $\beta_2 = 120°$, crack 1^a is initiated from the outer tip of fissure ① and crack 1^c is initiated from the outer tip of fissure ③. Crack 1^b quickly coalesces between the inner tips of fissures ① and ③. Note that cracks 1^a and 1^c propagate towards the edge of the specimen along the direction of axial stress.

The crack initiation mode in Fig. 10 appears very fast, which leads to an obvious stress drop in the axial stress–strain curve, except for $\beta_2 = 75°$. For example, the axial stress drops to 23.22 from 25.94 MPa for $\beta_2 = 90°$ and from 36.29 to 34.61 MPa for $\beta_2 = 105°$. However, for $\beta_2 = 75°$, although no distinct axial stress drop is observed, there is an obvious turning point (see point A of Fig. 6a) in the axial stress–strain curve.

Figure 11 depicts the effect of the ligament angle β_2 on the crack initiation stress of sandstone specimens containing three fissures ($\alpha = \beta_1 = 45°$) under uniaxial compression. The peak strength is also given in this figure for comparison. From Fig. 11, the crack initiation stress is distinctly lower than the peak strength for sandstone specimens containing three fissures. It is approximately 34% of the corresponding peak strength for $\beta_2 = 75°$ and 90°, and 46% of the corresponding peak strength for $\beta_2 = 105°$ and 120°. The crack initiation stress is nonlinearly related to β_2, and the effect of β_2 on the peak strength is approximately similar. As β_2 increases from 75° to 90°, the crack initiation stress decreases by 10% from 28.87 to 25.94 MPa, whereas it increases linearly from 25.94 to 47.91 MPa as β_2 increases from 90° to 120°.

4.2 Real-Time Crack Coalescence Process of Sandstone Specimens Containing Three Fissures ($\beta_2 = 75°$ and 90°)

Figures 12 and 13 present the real-time crack coalescence processes for sandstone specimens containing three fissures with $\beta_2 = 75°$ and 90°, respectively. As seen in Figs. 12 and 13, photographic monitoring can be used to identify and characterise the crack coalescence process. The letters denoted in Figs. 12 and 13 correspond to Fig. 6a, b, and the numbers represent the crack coalescence sequence during deformation (see Tables 3 and 4). The results for the flawed specimen containing three fissures ($\alpha = \beta_1 = 45°$, $\beta_2 = 90°$) are presented below to provide an example of the relationship between the real-time crack coalescence process and the axial stress–strain curve.

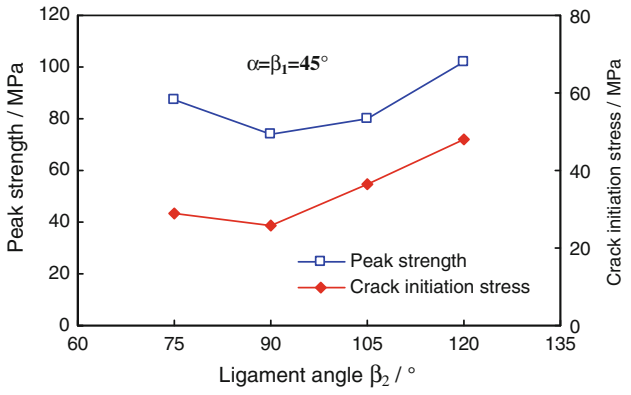

Fig. 11 Effect of the ligament angle β_2 on the crack initiation stress of sandstone specimens containing three fissures

In accordance with Fig. 13 and Table 4, the real-time crack coalescence behaviour of sandstone specimens containing three fissures ($\alpha = \beta_1 = 45°$, $\beta_2 = 90°$) is analysed for the entire deformation process, as shown in Fig. 6b. Before point A ($\sigma_1 = 25.94$ MPa $= 35.1\%\sigma_c$), the stress concentration at the inner and outer tips of the three fissures does not reach the material strength, and no crack is initiated. However, when the axial stress is loaded to point A, crack 1 induces rapidly from the inner and outer tips of fissures ① and ③, as shown in Fig. 10. The corresponding axial stress drops slightly from 25.94 to 23.22 MPa. After point A, the axial stress increases linearly with the strain to the elastic modulus of 27.11 GPa. For this moment, the length and width of crack 1 increase with the increasing axial deformation, and this occurrence can be inferred from point B ($\sigma_1 = 46.89$ MPa $= 63.5\%\sigma_c$) in Fig. 13. When the specimen is loaded to point C ($\sigma_1 = 47.54$ MPa $= 64.4\%\sigma_c$), crack 2^a quickly coalesces between the inner tip of fissure ② and the outer tip of fissure ③, and crack 2^b is initiated from the inner tip of fissure ② and evolves rapidly towards the top edge of the specimen along the direction of axial stress. This occurrence rapidly leads to a corresponding axial stress drop from 47.54 to 41.89 MPa. The continuous axial deformation increase (point D, $\sigma_1 = 43.46$ MPa) leads to the third stress drop from 43.46 to 38.87 MPa as a result of the coalescence of crack 3 between the inner tips of fissures ① and ③. The specimen still has a better supporting structure (Fig. 13d). Thus, with the increasing deformation, the axial supporting capacity also increases to an average modulus of approximately 25.15 GPa, which is slightly lower than the elastic modulus of 27.11 GPa. Because of the opening of crack 3, cracks 1^b and 1^c close but can still be seen by local magnification, as shown in Figs. 14a and 15.

Afterwards, when the specimen is loaded to point E ($\sigma_1 = 51.98$ MPa $= 70.4\%\sigma_c$), crack 4 is initiated from the outer tip of fissure ① and propagates towards the inner tip of fissure ③. However, it does not nucleate with the inner tip of fissure ③. The corresponding axial stress drops rapidly from 51.98 to 50.50 MPa, a minor drop compared with the previous two stress drops. The increasing displacement leads to the specimen being loaded to point F ($\sigma_1 = 52.57$ MPa $= 71.2\%\sigma_c$). Crack 5 is initiated at the outer tip of fissure ② and propagates towards the top edge of the specimen along

Fig. 12 Crack coalescence process of a sandstone specimen containing three fissures ($\alpha = \beta_1 = 45°$, $\beta_2 = 75°$) under uniaxial compression. The *letters* correspond to those shown in Fig. 6a

the direction of axial stress, resulting in a rapid axial stress drop from 52.57 to 49.49 MPa. At this time, the specimen still has a good supporting structure (Fig. 13f). Therefore, with the increase of axial deformation, the axial supporting capacity begins to increase with an approximately equal modulus of 25.39 GPa as the previous average modulus of 25.15 GPa, revealing that the initiation and coalescence of cracks 4 and 5 do not affect the deformation behaviour of the specimen. When the specimen is loaded to point G ($\sigma_1 = 62.44$ MPa $= 84.5\%\sigma_c$), crack 6 emanates towards the top edge of the specimen from the outer tip of fissure ① along the direction of axial stress, leading to a minor axial stress drop from 62.44 to 61.14 MPa. For the moment, the axial stress begins to increase slowly as the axial deformation increases. As a result of obvious damage to the supporting structure (Fig. 13g), the reloading average modulus of 22.8 GPa is distinctly lower than the elastic modulus of 27.11 GPa. Moreover, the axial stress–strain curve of the specimen departs towards the strain axis when the deformation approaches the peak strain. The continuous deformation increase leads to the specimen being loaded to peak point H ($\sigma_1 = 73.87$ MPa $= 100\%\sigma_c$). At this moment, crack 7 is initiated at the outer tip of fissure ① and evolves towards the inner tip of fissure ③. The corresponding axial stress of the specimen begins to decrease slowly as the deformation increases. When the axial stress of the specimen decreases to point I ($\sigma_1 = 71.25$ MPa), crack 8 emanates from the outer tip of fissure ② and propagates towards the top edge of the specimen along the direction of axial stress, and the corresponding axial stress drops to 70.57 MPa. It should be noted that Fig. 16 shows the local magnification of several cracks. From Fig. 16, it is very clear that, near to the outer tip of fissure ②, many minor microscopic cracks are observed, which probably result

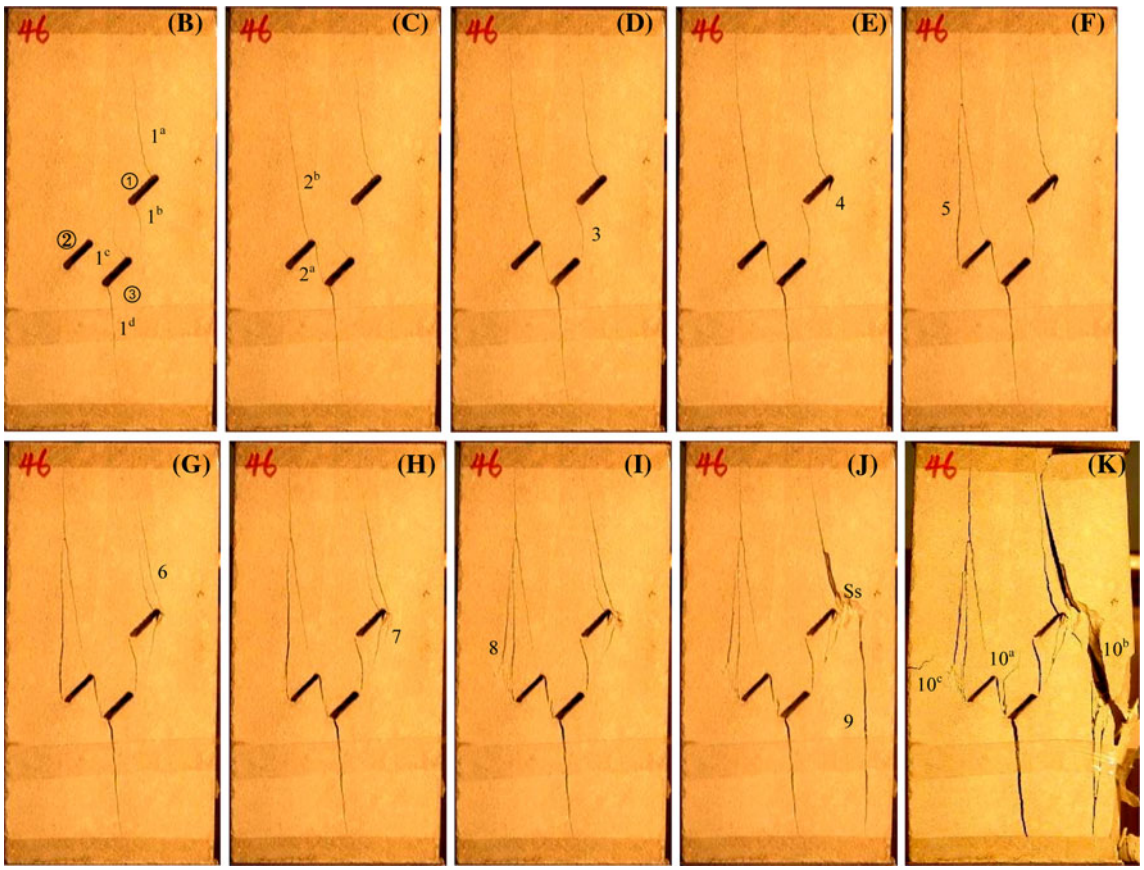

Fig. 13 Crack coalescence process of sandstone specimens containing three fissures ($\alpha = \beta_1 = 45°$, $\beta_2 = 90°$) under uniaxial compression. The *letters* correspond to those shown in Fig. 6b

Table 3 Crack coalescence behaviour of a sandstone specimen containing three fissures ($\alpha = \beta_1 = 45°$, $\beta_2 = 75°$)

Coalescence point	Initiated cracks	ε_1 ($\times 10^{-3}$)	σ_1 (MPa)	Stress drop (MPa)
B	No new cracks	1.774	34.50	No
C	No new cracks	2.592	59.76	No
D	Crack 2	2.618	60.48	57.19
E	Crack 3	2.625	57.52	51.30
F	Crack 4	3.292	68.82	62.31
G	Crack 5	3.757	73.61	67.92
H (peak strength)	No new cracks	4.568	87.17	86.97
I	Crack 6	4.690	0.168	Ultimate failure

Table 4 Crack coalescence behaviour of a sandstone specimen containing three fissures ($\alpha = \beta_1 = 45°$, $\beta_2 = 90°$)

Coalescence point	Initiated cracks	ε_1 ($\times 10^{-3}$)	σ_1 (MPa)	Stress drop (MPa)
B	No new cracks	2.548	46.89	No
C	Crack 2	2.572	47.54	41.89
D	Crack 3	2.637	43.46	38.87
E	Crack 4	3.191	51.98	50.50
F	Crack 5	3.273	52.57	49.49
G	Crack 6	3.804	62.44	61.14
H (peak strength)	Crack 7	4.464	73.87	73.74
I	Crack 8	4.549	71.25	70.57
J	Crack 9	4.601	69.42	47.99
K	Crack 10	4.708	0.148	Ultimate failure

from the local compressive stress concentration. The continuous deformation increase leads to the axial stress dropping to point J ($\sigma_1 = 69.42$ MPa). At this time, crack 9 forms rapidly in the bottom right region of the specimen near the outer tip of fissure ①, and the coalescence direction is approximately parallel to the axial stress. Therefore, the axial supporting capacity drops rapidly to 47.99 MPa in an approximately constant axial strain. During the coalescence of crack 9, some surface failures are observed. Ultimate brittle failure then occurs quickly and crack 10 emanates, resulting in a rapid reduction of the axial stress to 0.15 MPa.

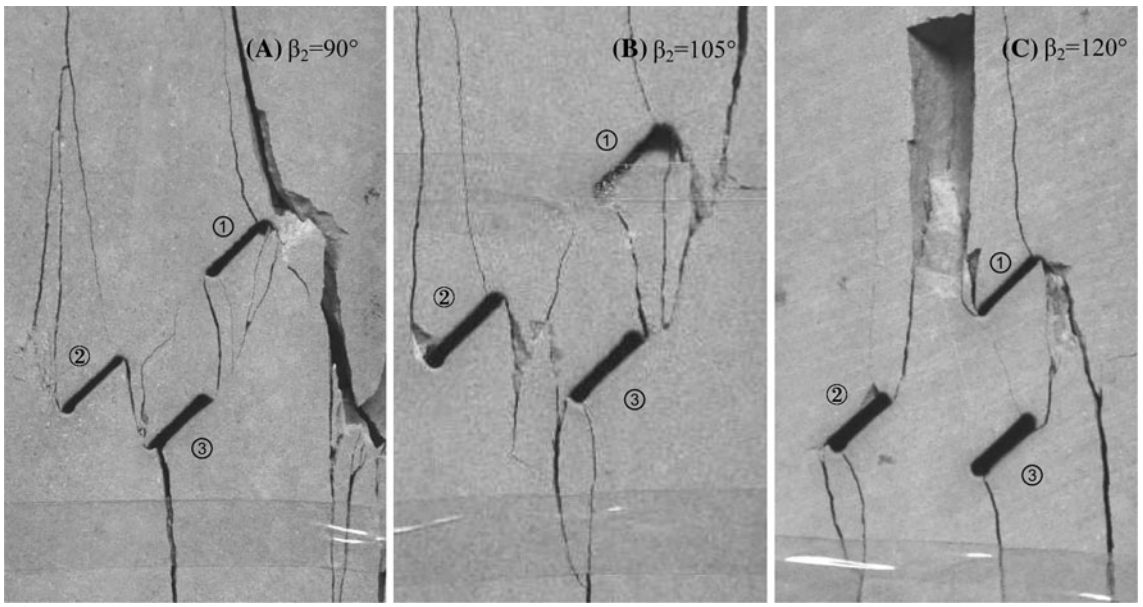

Fig. 14 Local magnification of the ultimate failure mode of sandstone specimens containing three fissures ($\alpha = \beta_1 = 45°$, $\beta_2 = 90°$, 105° and 120°) under uniaxial compression

At this point, the specimen can no longer support the axial stress.

In accordance with the microscopic observations after failure of the specimen shown in Figs. 15 and 16, we can see that the crack coalescence path is a zig-zag under local magnification, e.g. cracks 1^b and 1^c, which results mainly from the effect of the grain scale in the tested sandstone material on the crack coalescence path. The width of cracks 1^b and 1^c is very small, of about 40–50 μm. The width of crack 3 reaches about 500–600 μm, which is distinctly higher than that of cracks 1^b and 1^c. However, the width of crack 2 is about 800–1,000 μm. Therefore, different cracks have different widths. Even for the same crack, the width is different along the direction of its length during loading.

4.3 Real-Time Crack Coalescence Process of Sandstone Specimens Containing Three Fissures ($\beta_2 = 105°$ and 120°)

Figures 17 and 18 present the real-time crack coalescence process of sandstone specimens containing three fissures with $\beta_2 = 105°$ and 120°, respectively. Figure 14b, c show the corresponding, locally magnified images of the ultimate failure mode of the specimens. The letters denoted in Figs. 17 and 18 correspond to Fig. 6c, d, and the numbers represent the crack coalescence sequence during the entire deformation (see Tables 5 and 6). Here, results from the flawed specimen containing three fissures ($\alpha = \beta_1 = 45°$, $\beta_2 = 120°$) are presented to provide an example of the relationship between the real-time crack coalescence process and the axial stress–strain curve for specimens with overlapping fissure geometry (fissures ① and ③).

Compared with the real-time crack coalescence process of the flawed specimen containing three fissures ($\alpha = \beta_1 = 45°$, $\beta_2 = 90°$), the process of the flawed specimen containing three fissures ($\alpha = \beta_1 = 45°$, $\beta_2 = 120°$) was distinctly different. Therefore, the difference between the effects of the real-time crack coalescence process on the axial stress–strain curve was also larger.

In accordance with Fig. 18 and Table 6, the real-time crack coalescence behaviours of sandstone specimens containing three fissures ($\alpha = \beta_1 = 45°$, $\beta_2 = 120°$) are analysed during the entire deformation, as shown in Fig. 6d. Before point A ($\sigma_1 = 47.91$ MPa $= 47\%\sigma_c$), the stress concentration at the inner and outer tips of the three fissures does not reach the material strength, and no crack is induced. However, when the axial stress is loaded to point A, crack 1 rapidly forms from the inner and outer tips of fissures ① and ③, as shown in Fig. 10. The corresponding axial stress drops slightly from 47.91 to 46.12 MPa. After point A, the axial stress increases linearly with the increasing axial deformation to the elastic modulus of 32.21 GPa. The width of crack 1 also increases, while the length of crack 1 does not increase because of the boundary limitations of the specimen, as shown by point B ($\sigma_1 = 65.10$ MPa $= 63.9\%\sigma_c$) in Fig. 18. When the specimen is loaded to point C ($\sigma_1 = 71.14$ MPa $= 69.8\%\sigma_c$), crack 2 is initiated from the outer tip of fissure ① and propagates towards the inner tip of fissure ③ along the direction of axial stress. This occurrence does not lead to

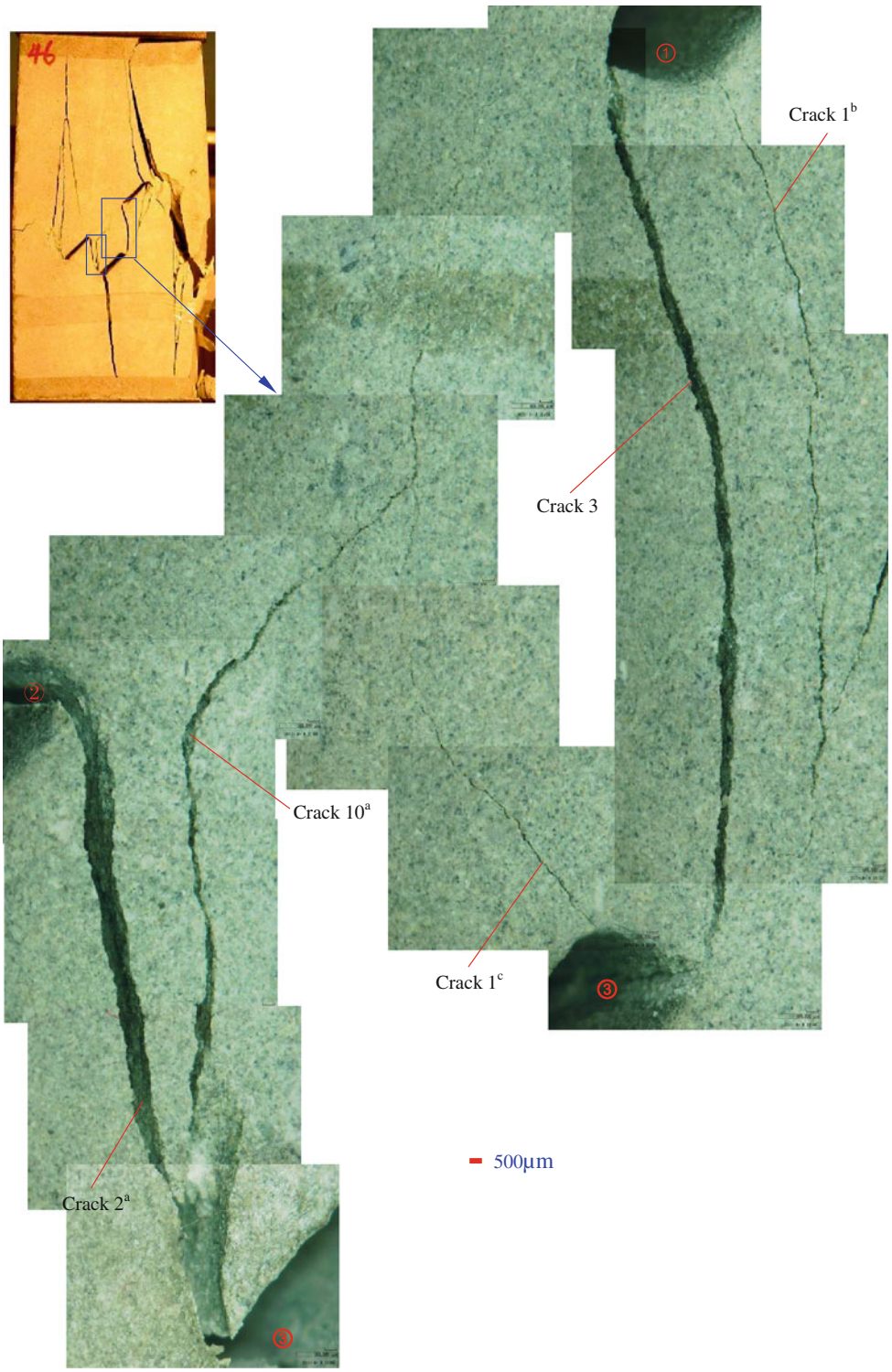

Fig. 15 Microscopic observation of several crack coalescences between fissures ①, ② and ③ of a sandstone specimen containing three fissures ($\alpha = \beta_1 = 45°$, $\beta_2 = 90°$) after failing under uniaxial compression

an obvious axial stress drop and the stress changes from 71.14 to 70.45 MPa. The continuous axial deformation increase (point D, $\sigma_1 = 81.47$ MPa) does not result in new cracks, but the width of cracks 1 and 2 slightly increase. Crack 2 does not coalesce to the inner tip of fissure ③. The specimen still has a better supporting structure (Fig. 18d). Thus, with the increase of axial deformation, the axial stress of the specimen increases to an approximate average modulus of 31.73 GPa, similar to the elastic modulus of 32.21 GPa. When the specimen is loaded to point E

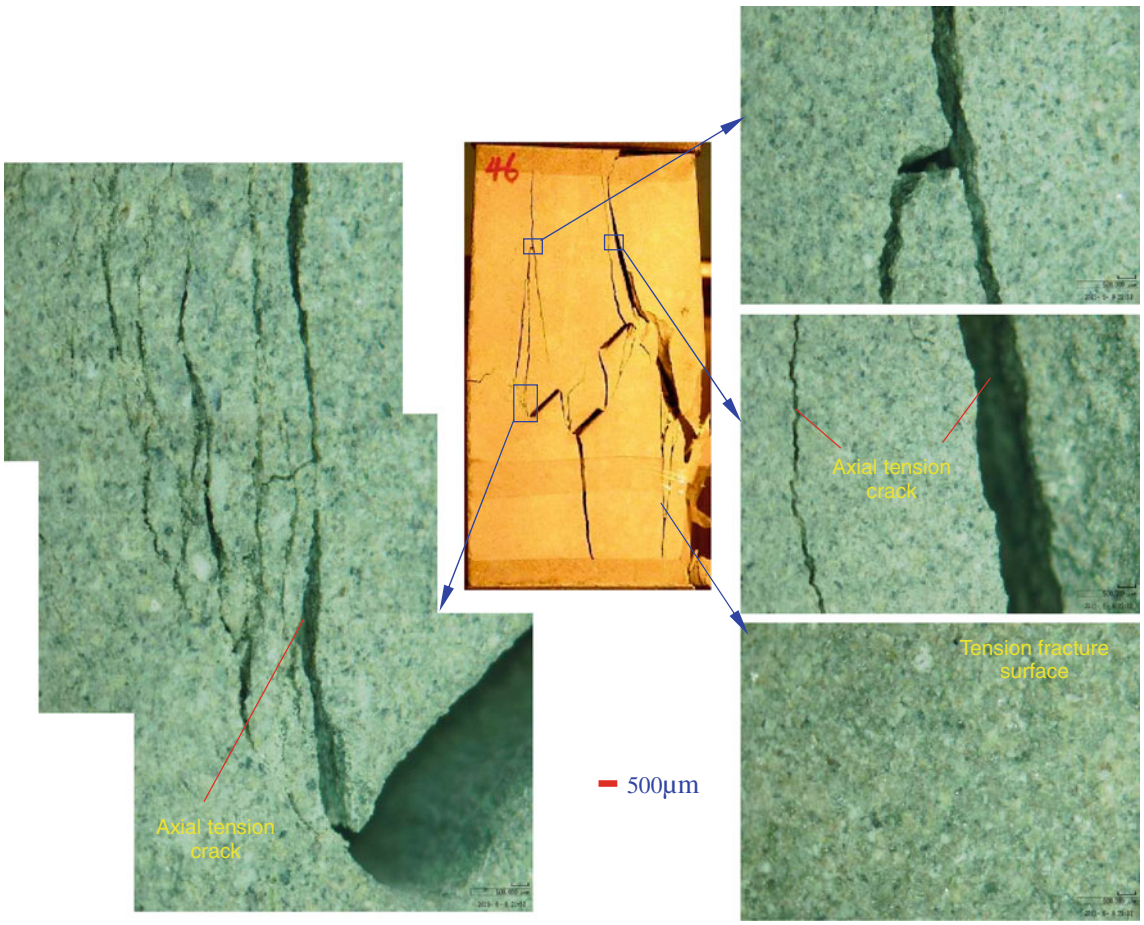

Fig. 16 Microscopic observation of several crack coalescences of a sandstone specimen containing three fissures ($\alpha = \beta_1 = 45°$, $\beta_2 = 90°$) under uniaxial compression

($\sigma_1 = 86.37$ MPa $= 84.8\%\sigma_c$), crack 2 coalesces rapidly to the inner tip of fissure ③, and its width increases substantially, while crack 1^b closes. In the above process, the axial stress drops from 86.37 to 85.49 MPa. Afterwards, the axial stress increases linearly with the increasing deformation to the average modulus of 32.56 GPa, which is approximately equal to the elastic modulus of 32.21 GPa.

When the specimen is loaded to point F ($\sigma_1 = 99.59$ MPa $= 97.8\%\sigma_c$), crack 3^a emanates from the inner tip of fissure ① and propagates towards the top edge of the specimen along the direction of axial stress. However, cracks 3^b and 3^c are initiated from the outer and inner tips of fissure ②, respectively, and propagate along the direction of axial stress. Notably, the width of crack 3^a is greater than that of cracks 3^b and 3^c. The corresponding axial stress drops rapidly from 99.59 to 95.58 MPa. Afterwards, with the increasing deformation, the specimen experiences two minor stress drops as a result of the emanation of cracks 4 and 5 in the specimen. The axial stress–strain curve departs towards the strain axis during the coalescence process of cracks 4 and 5. The continuous increase of deformation results in the specimen being loaded to peak point I ($\sigma_1 = 101.86$ MPa $= 100\%\sigma_c$). At this moment, the width and length of cracks 3–5 increase with the increasing axial deformation, and crack 1^a closes. Moreover, some surface failures are observed between cracks 3^a and 4. Although no new crack is observed, there is an obvious stress drop from 101.86 to 78.76 MPa in an approximately constant axial strain. Ultimate brittle failure is then quickly induced, and crack 6 is initiated as a result of the rapid reduction of the axial stress to 7.2 MPa.

Figures 19 and 20 show some microscopic observations of crack coalescence in the flawed sandstone specimens containing three fissures ($\alpha = \beta_1 = 45°$, $\beta_2 = 105°$) under uniaxial compression. Open tensile cracks are very clear and the path of crack coalescence follows a pronounced zig-zag shape as shown with local magnification. Tensile cracks can also be further testified by the tensile fracture surface shown in Fig. 19. From Fig. 20, the maximum width of crack 1^b reaches about 1,500 μm, whereas crack 1^c is very fine compared with crack 1^b.

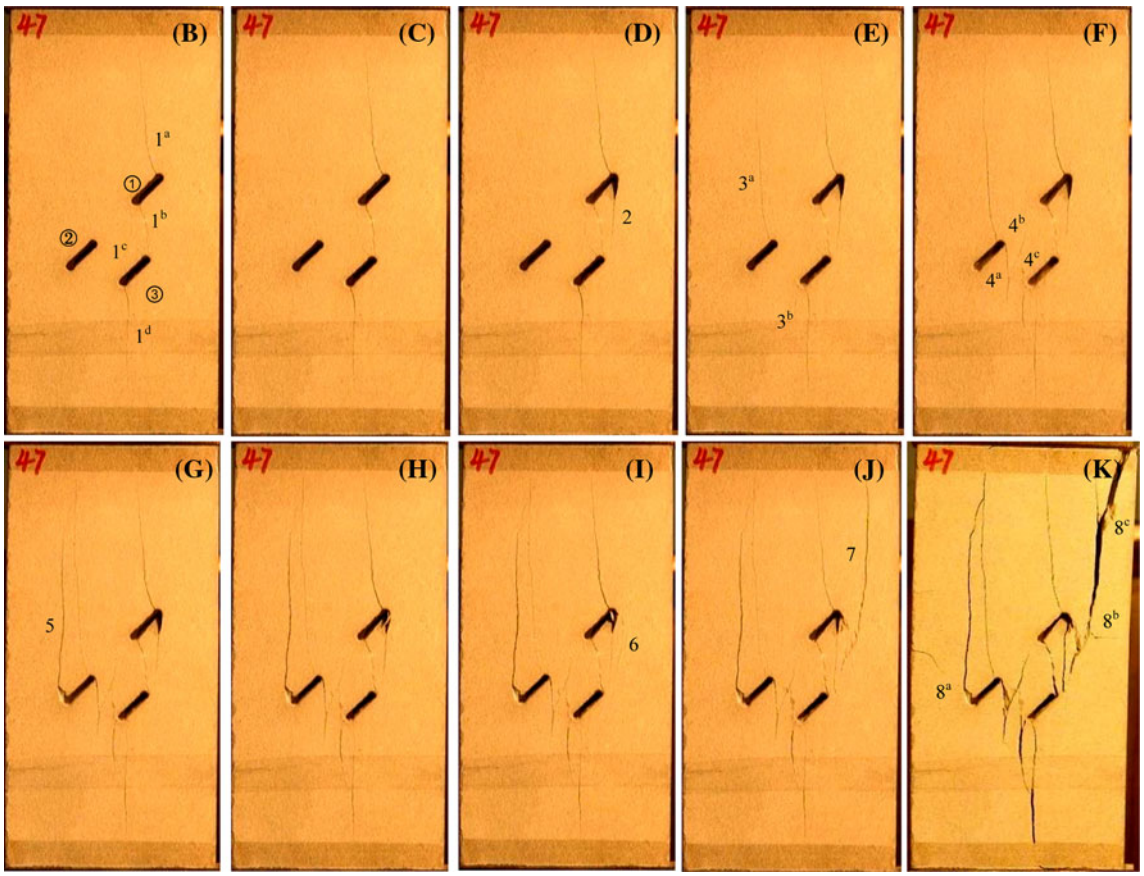

Fig. 17 Crack coalescence process of a sandstone specimen containing three fissures ($\alpha = \beta_1 = 45°$, $\beta_2 = 105°$) under uniaxial compression. The denoted *letters* correspond to those shown in Fig. 6c

5 Crack Coalescence Type and Strain Evolution Analysis

5.1 Crack Coalescence Type Analysis

Figure 21 depicts a sketch of the initiated crack coalescence types for sandstone specimens containing three fissures. Although the crack coalescence types for the specimens in this study were the same as those observed in a previous study (Yang and Jing 2011), each flawed specimen with three fissures had different crack coalescence types as a result of the different flaw geometries. Table 7 summarises the initiated crack coalescence types of sandstone specimens containing three fissures ($\alpha = \beta_1 = 45°$). The crack coalescence modes are also plotted in Table 7.

In accordance with Table 7, no crack coalescence occurs between fissures ① and ② in the flawed specimens containing three fissures ($\alpha = \beta_1 = 45°$), whereas crack coalescence occurs between fissures ① and ③, and ② and ③, but not between fissures ② and ③ for a specimen with $\beta_2 = 120°$. Tensile wing crack, secondary tensile crack and far-field crack are observed in all flawed specimens containing three fissures ($\alpha = \beta_1 = 45°$). Shear crack and lateral crack are only observed between fissures ① and ③ in flawed specimens with $\beta_2 = 75°$, while compressive crack is observed between fissures ② and ③ in flawed specimens with $\beta_2 = 75°$ and 90°. However, an anti-tensile crack is observed in flawed specimens with $\beta_2 = 90°$, 105° and 120°. Surface spalling is observed in all flawed specimens as a result of the brittleness of the sandstone material and the local concentration of compression.

5.2 Strain Evolution Analysis

Using the digital image correlation technique and analysing the images captured during loading, the full-field strain of the specimen surface is obtained. In this research, the images are analysed with the software CMV, developed at École Polytechnique, Paris, France (Yang et al. 2011). The transformation gradients are averaged over the domain of interest (4.4 × 4.4 mm) to determine the strains.

The following equation for equivalent strain is used to study the mechanical behaviour:

$$\text{Equivalent strain} = \sqrt{2/3 e_{ij} e_{ij}} \quad (1)$$

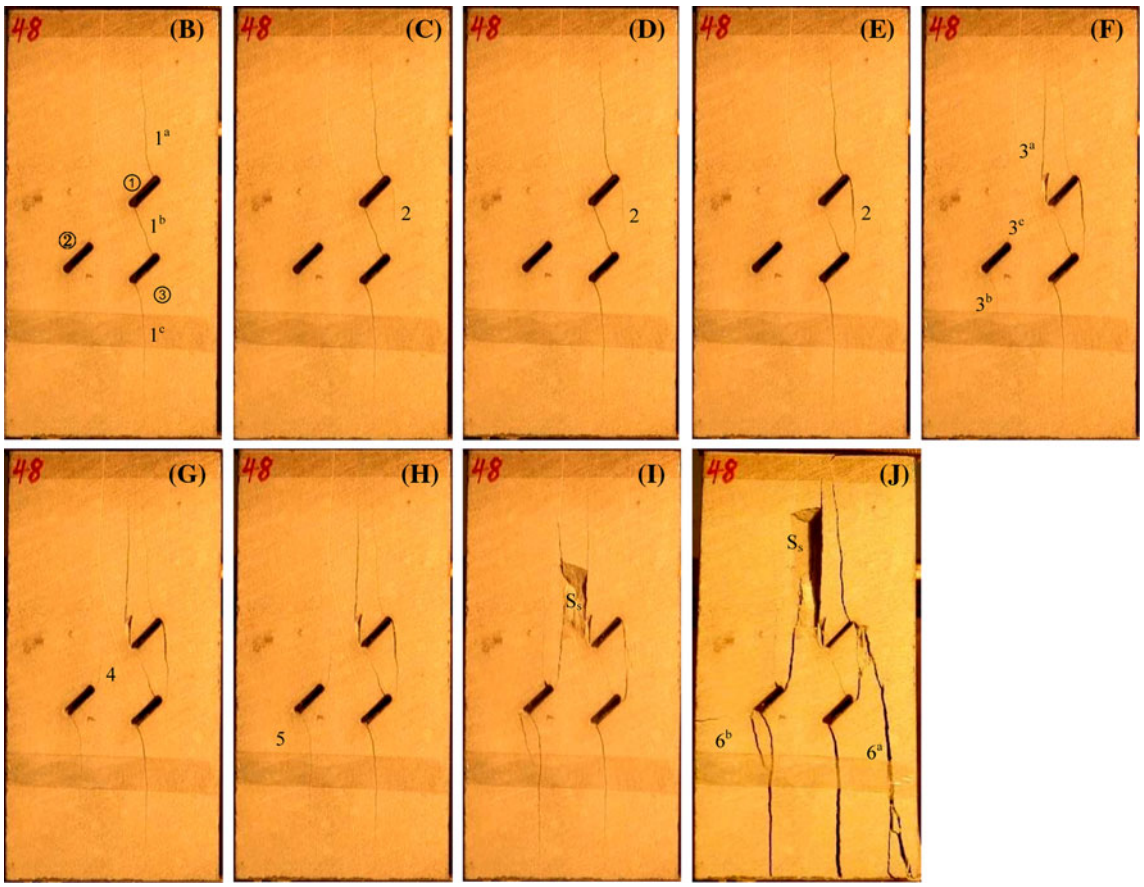

Fig. 18 Crack coalescence process of a sandstone specimen containing three fissures ($\alpha = \beta_1 = 45°$, $\beta_2 = 120°$) under uniaxial compression. The denoted *letters* correspond to those shown in Fig. 6d

Table 5 Crack coalescence behaviour of a sandstone specimen containing three fissures ($\alpha = \beta_1 = 45°$, $\beta_2 = 105°$)

Coalescence point	Initiated cracks	ε_1 ($\times 10^{-3}$)	σ_1 (MPa)	Stress drop (MPa)
B	No new cracks	2.449	51.98	No
C	No new cracks	3.272	78.22	No
D	Crack 2	3.308	79.46	77.66
E (peak strength)	Crack 3	3.387	79.71	77.88
F	Crack 4	3.387	77.88	64.64
G	Crack 5	3.404	64.64	58.54
H	No new cracks	3.845	67.89	No
I	Crack 6	3.967	69.58	No
J	Crack 7	3.996	69.82	59.36
K	Crack 8	4.277	2.1	Ultimate failure

Table 6 Crack coalescence behaviour of a sandstone specimen containing three fissures ($\alpha = \beta_1 = 45°$, $\beta_2 = 120°$)

Coalescence point	Initiated cracks	ε_1 ($\times 10^{-3}$)	σ_1 (MPa)	Stress drop (MPa)
B	No new cracks	2.776	65.10	No
C	Crack 2	2.978	71.14	70.45
D	No new cracks	3.303	81.47	No
E	No new cracks	3.457	86.37	85.49
F	Crack 3	3.915	99.59	95.58
G	Crack 4	4.022	98.66	98.36
H	Crack 5	4.079	99.56	98.74
I (peak strength)	No new cracks	4.254	101.86	78.76
J	Crack 6	4.315	7.26	Ultimate failure

where e_{ij} is the deviatoric strain. Here, the results for specimens containing three fissures ($\alpha = \beta_1 = 45°$, $\beta_2 = 90°$) are presented to demonstrate the strain evolution analysis for pre-cracked brittle sandstone. Because several large cracks are created during loading and because these zones become new subsets that cannot be identified in the undeformed image, reference images are taken at different states (stress at 0, 51.98 and 63.08 MPa). The equivalent strain evolution under mechanical loading is illustrated in Figs. 22 and 23.

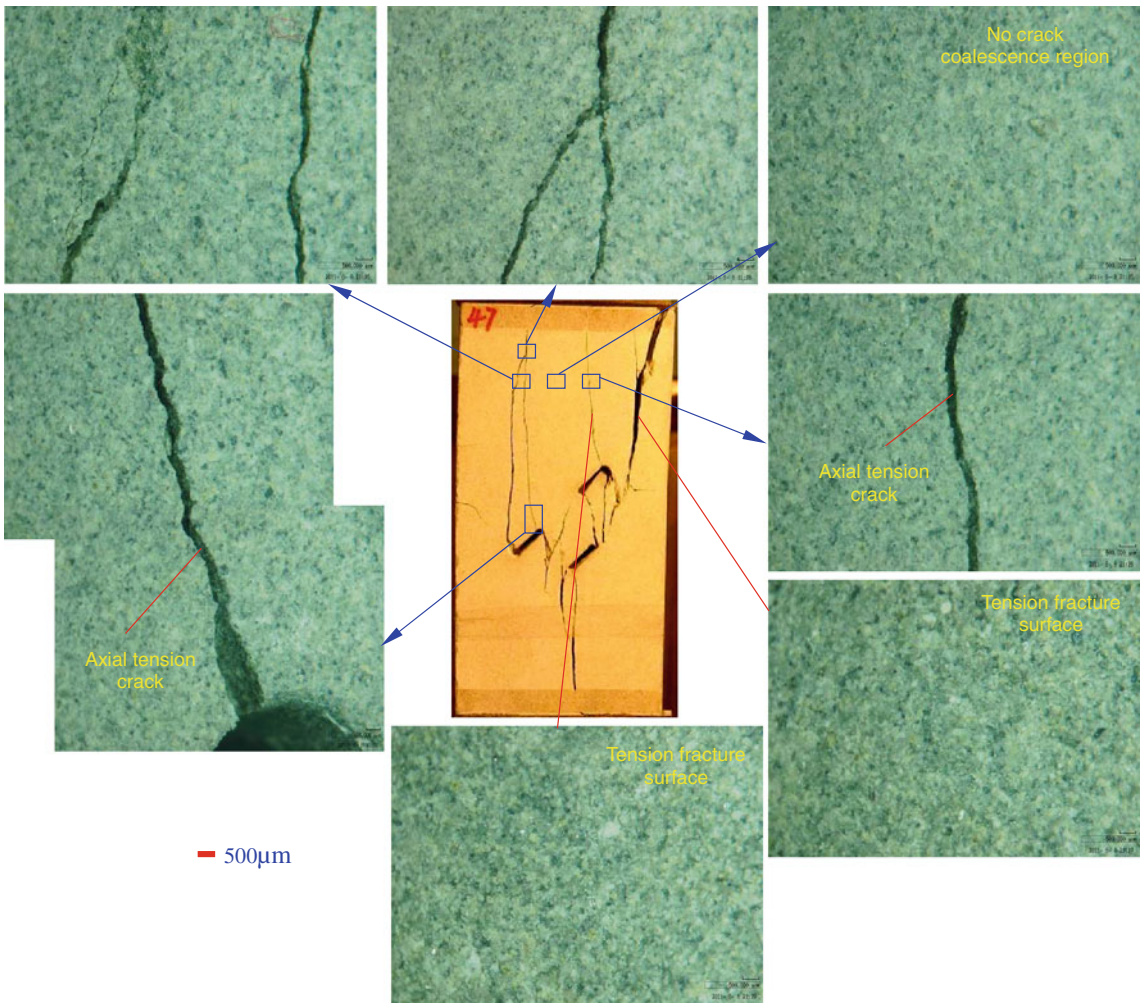

Fig. 19 Microscopic observation of several crack coalescences of a sandstone specimen containing three fissures ($\alpha = \beta_1 = 45°$, $\beta_2 = 105°$) under uniaxial compression

The full-field strain clearly shows that the strain at the intact zone is relatively homogeneous (e.g. zone A in Fig. 22a) and that strain localisation mainly occurs around the pre-created fissures (e.g. zone B in Fig. 22b) and develops along the new cracks (e.g. zone C in Figs. 22 and 23). While the axial stress increases to 25.94 MPa, several new micro-cracks appear, and this level of stress is regarded to be the threshold for damage. The direction of the new crack around the pre-existing fissures is approximately perpendicular to the latter and is probably related to the maximal tension in this direction.

6 Conclusions

We conducted uniaxial compression tests on brittle sandstone specimens, with dimensions of 80 × 160 × 30 mm, containing three pre-existing open fissures in order to investigate the effect of the ligament angle β_2 on the fracture coalescence behaviour of sandstone specimens.

The influence of the ligament angle β_2 on the crack initiation stress, peak strength and peak strain of sandstone specimens containing three fissures is determined. The peak strength and peak strain of flawed specimens containing three fissures are lower than those of intact specimens. To indicate the reduction extent of the peak strength of flawed specimens containing three fissures compared with intact specimens, a reduction factor is proposed. The crack initiation stress is non-linearly related to β_2, and the effect of β_2 on the peak strength is approximately the same. The crack initiation stress and peak strength first decrease and then increase as β_2 increases in the range from 75° to 120°. The crack initiation stress is distinctly lower than the peak strength for sandstone specimens containing three fissures; the peak strength is approximately 34% lower for $\beta_2 = 75°$ and 90°, while it is 46% of the corresponding peak strength for $\beta_2 = 105°$ and 120°.

The crack initiation mode of brittle sandstone specimens containing three fissures ($\alpha = \beta_1 = 45°$) under uniaxial

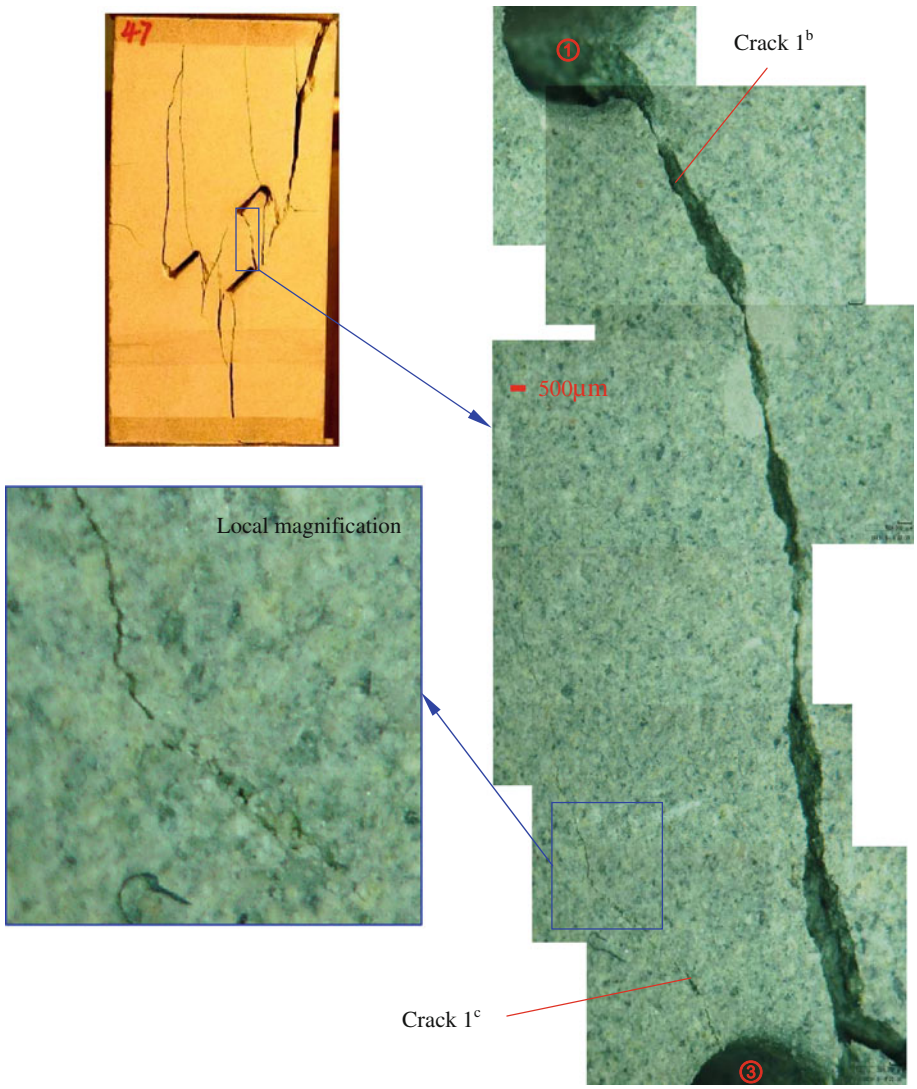

Fig. 20 Microscopic observation of crack coalescences between fissures ① and ③ of a sandstone specimen containing three fissures ($\alpha = \beta_1 = 45°$, $\beta_2 = 105°$) after failing under uniaxial compression

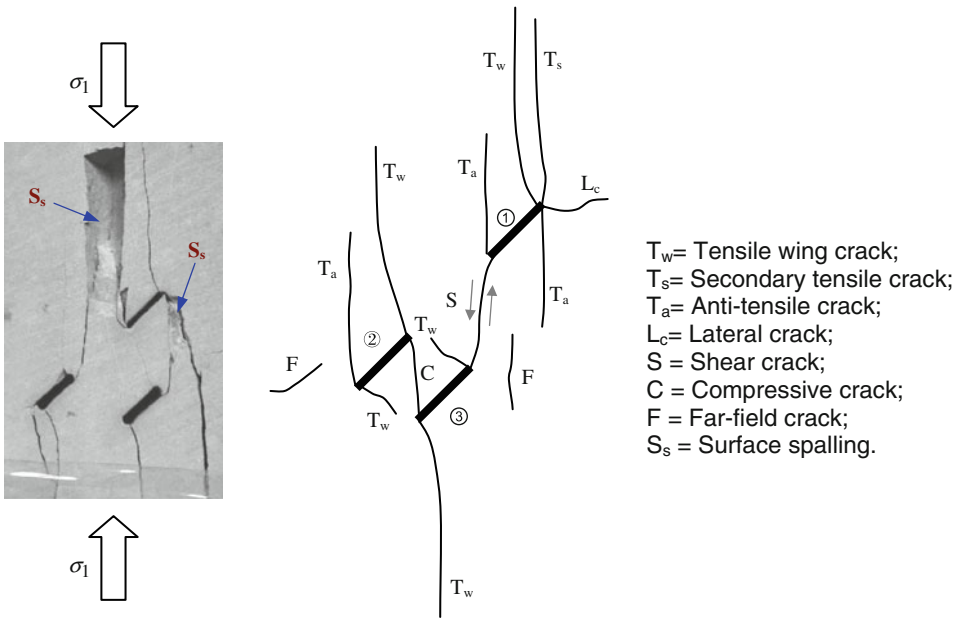

Fig. 21 A sketch of the initiated crack coalescence types of sandstone specimens containing three fissures

Table 7 Crack coalescence mode and type of sandstone specimens containing three fissures ($\alpha = \beta_1 = 45°$)

β_2	Fissure ①③	Fissure ②③	Fissure ①②	Fissures ①②③	Crack coalescence type description
75°	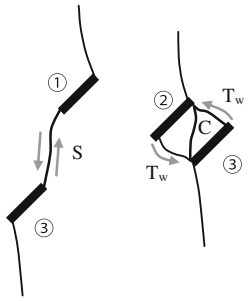		No coalescence	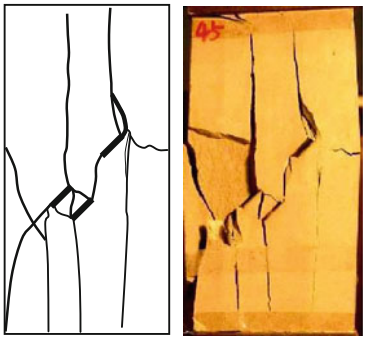	T_w: Crack 1^a-1^d, 2^b. T_s: Crack 4. S: Crack 3. C: Crack 2^a. L_c: Crack 6^b. F: Crack 5, 6^a, 6^c. S_s: √more.
90°	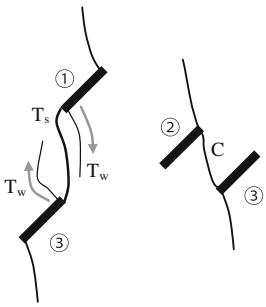		No coalescence	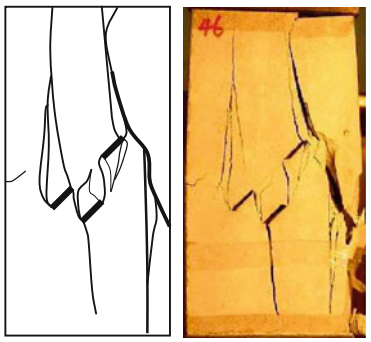	T_w: Crack 1^a-1^d, 2^b. T_s: Crack 3, 6-8, 9, 10^a, 10^b. T_a: Crack 4-5. C: Crack 2^a. F: Crack 10^c. S_s: √small.
105°	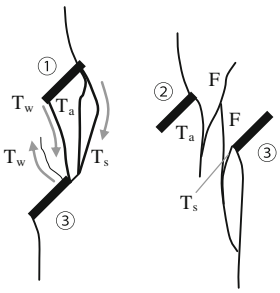	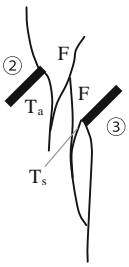	No coalescence	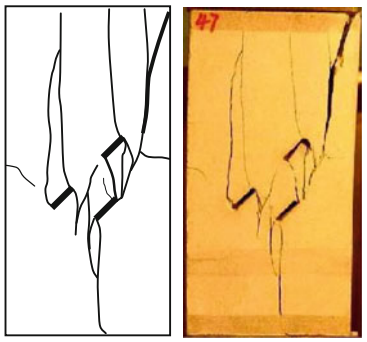	T_w: Crack 1^a-1^d, 3^a. T_s: Crack 3^b, 6. T_a: Crack 2, 4^a, 5. F: Crack 4^b, 4^c, 7, 8^a-8^c. S_s: √small.
120°	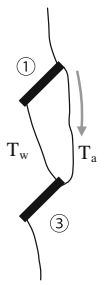	No coalescence	No coalescence	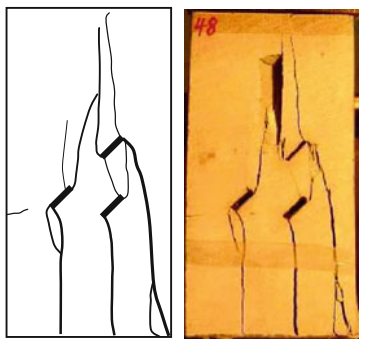	T_w: Crack 1^a-1^c, 3^b-3^c. T_s: Crack 4-5, 6^a. T_a: Crack 2, 3^a. F: Crack 6^b. S_s: √more.

The numbers correspond to those shown in Figs. 12, 13, 17, 18

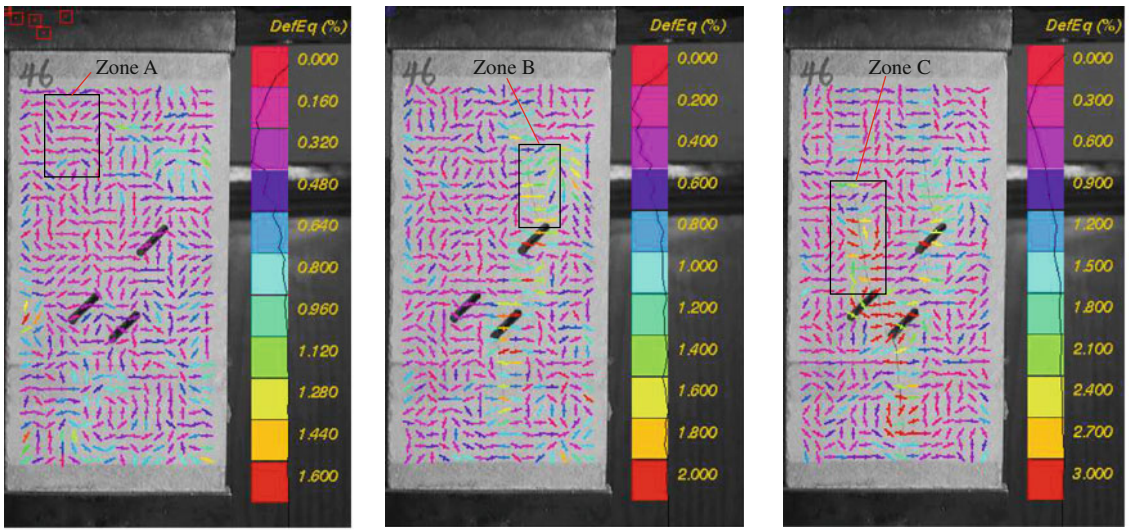

(A) The axial stress increased from 0 MPa to 25.94 MPa

(B) The axial stress increased from 0 MPa to 32.44 MPa

(C) The axial stress increased from 0 MPa to 47.54 MPa

Fig. 22 Equivalent strain evolution with increasing axial stress: **a** from 0 to 25.94 MPa; **b** from 0 to 32.44 MPa; **c** from 0 to 47.54 MPa

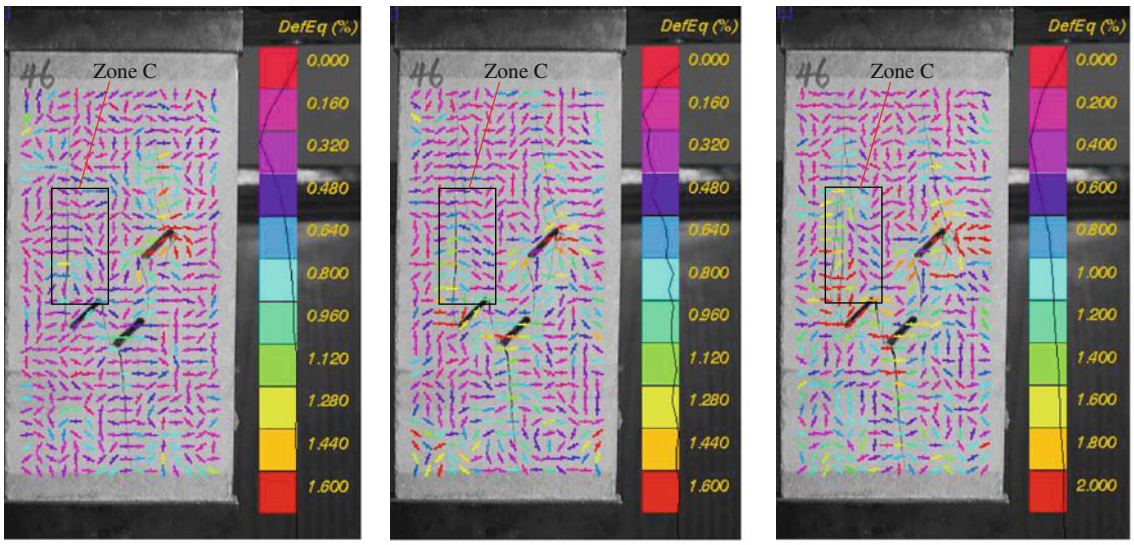

(A) The axial stress increased from 51.98 MPa to 63.08 MPa

(B) The axial stress increased from 63.08 MPa to 73.87 MPa

(C) The axial stress increased from 63.08 MPa to rupture

Fig. 23 Equivalent strain evolution with increasing axial stress: **a** from 51.98 to 63.08 MPa; **b** from 63.08 to 73.87 MPa; **c** from 63.08 MPa to rupture

compression is analysed and determined to be dependent on β_2. For $\beta_2 = 75°$, crack 1 is initiated from the inner and outer tips of fissures ② and ③, while no crack is initiated from the inner and outer tips of fissure ①. For $\beta_2 = 90°$ and 105°, the crack initiation mode is different from that of the other three specimens. Crack 1 initiates from the inner and outer tips of fissures ① and ③, while no crack is initiated from the inner and outer tips of fissure ②. For $\beta_2 = 120°$, crack 1^a initiates from the outer tip of fissure ① and crack 1^c is initiated from the outer tip of fissure ③. However, crack 1^b quickly coalesces between the inner tips of fissures ① and ③.

To confirm the sequence of crack coalescence in brittle sandstone specimens containing three fissures ($\alpha = \beta_1 = 45°$), a photographic monitoring technique is used throughout the entire process of deformation failure. According to the monitored results, the relationship between the real-time crack coalescence process and the axial stress–strain curve

of the specimens is also obtained, which can be used to evaluate the macroscopic deformation failure characteristics of pre-cracked rock materials.

The crack coalescence modes of sandstone specimens containing three fissures ($\alpha = \beta_1 = 45°$) are analysed using initiated crack coalescence types from a previous study, including tensile wing crack, anti-tensile crack, lateral crack, shear crack, compressive crack, far-field crack, surface spalling and secondary tensile crack. No crack coalescence occurs between fissures ① and ② in the flawed specimens. However, crack coalescence occurs between fissures ① and ③, and ② and ③, but not between fissures ② and ③ for a specimen with $\beta_2 = 120°$. Tensile wing crack, secondary tensile crack, far-field crack and surface spalling are observed in all flawed specimens. Shear crack and lateral crack are only observed between fissures ① and ③ in the flawed specimens with $\beta_2 = 75°$, while compressive crack is observed between fissures ② and ③ in flawed specimens with $\beta_2 = 75°$ and 90°. Anti-tensile crack is observed in flawed specimens with $\beta_2 = 90°$, 105° and 120°.

The equivalent strain evolution fields of specimens with $\alpha = \beta_1 = 45°$, $\beta_2 = 90°$ are obtained using the digital image correlation technique, and the results agree with the experimental results for pre-cracked brittle sandstone. The full-field strain clearly shows that the strain at the intact zone is relatively homogeneous and that strain localisation mainly occurs around the pre-created fissures and develops along the new cracks. The direction of the new crack around the pre-existing fissures is nearly perpendicular to the latter and is probably related to the maximal tension in this direction.

Acknowledgments This research was supported by the National Natural Science Foundation of China (Grant Nos. 51179189 and 51074162), a China Postdoctoral Science Foundation funded project (Grant Nos. 201104585 and 20100470068) and Jiangsu Planned Projects for Postdoctoral Research Funds (Grant No. 1002027C). We would also like to express our sincere gratitude to the editor and the two anonymous reviewers for their valuable comments, which have greatly improved this paper.

References

Chang S-H, Lee C-I (2004) Estimation of cracking and damage mechanisms in rock under triaxial compression by moment tensor analysis of acoustic emission. Int J Rock Mech Min Sci 41:1069–1086

Debecker B, Vervoort A (2009) Experimental observation of fracture patterns in layered slate. Int J Fract 159:51–62

Feng X-T, Ding WX, Zhang DX (2009) Multi-crack interaction in limestone subject to stress and flow of chemical solutions. Int J Rock Mech Min Sci 46(1):159–171

Hoek E (1998) Practical rock engineering. Department of Civil Engineering, University of Toronto. Rocscience Inc., Toronto, Ontario, Canada

Janeiro RP, Einstein HH (2010) Experimental study of the cracking behavior of specimens containing inclusions (under uniaxial compression). Int J Fract 164(1):83–102

Lee H, Jeon S (2011) An experimental and numerical study of fracture coalescence in pre-cracked specimens under uniaxial compression. Int J Solids Struct 48(6):979–999

Li Y-P, Chen L-Z, Wang Y-H (2005) Experimental research on pre-cracked marble under compression. Int J Solids Struct 42(9–10): 2505–2516

Park CH, Bobet A (2009) Crack coalescence in specimens with open and closed flaws: a comparison. Int J Rock Mech Min Sci 46(5): 819–829

Prudencio M, Van Sint Jan M (2007) Strength and failure modes of rock mass models with non-persistent joints. Int J Rock Mech Min Sci 44(6):890–902

Tang CA, Lin P, Wong RHC, Chau KT (2001) Analysis of crack coalescence in rock-like materials containing three flaws—part II: numerical approach. Int J Rock Mech Min Sci 38(7):925–939

Tham LG, Liu H, Tang CA, Lee PKK, Tsui Y (2005) On tension failure of 2-D rock specimens and associated acoustic emission. Rock Mech Rock Eng 38(1):1–19

Wong LNY, Einstein HH (2009a) Crack coalescence in molded gypsum and Carrara marble: part 1. Macroscopic observations and interpretation. Rock Mech Rock Eng 42(3):475–511

Wong LNY, Einstein HH (2009b) Systematic evaluation of cracking behavior in specimens containing single flaws under uniaxial compression. Int J Rock Mech Min Sci 46(2):239–249

Wong RHC, Chau KT, Tang CA, Lin P (2001) Analysis of crack coalescence in rock-like materials containing three flaws—part I: experimental approach. Int J Rock Mech Min Sci 38(7):909–924

Yang S-Q, Jing H-W (2011) Strength failure and crack coalescence behavior of brittle sandstone samples containing a single fissure under uniaxial compression. Int J Fract 168(2):227–250

Yang DS, Bornert M, Chanchole S, Wang LL, Valli P, Gatmiri B (2011) Experimental investigation of the delayed behavior of unsaturated argillaceous rocks by means of digital image correlation techniques. Appl Clay Sci 53(1):53–62